Primary instabilities and bicriticality in flow between counter-rotating cylinders

W. F. Langford,[a] Randall Tagg, Eric J. Kostelich, Harry L. Swinney, and
Martin Golubitsky[b]

Department of Physics and the Center for Nonlinear Dynamics, The University of Texas, Austin, Texas 78712

The primary instabilities and bicritical curves for flow between counter-rotating cylinders have been computed numerically from the Navier–Stokes equations assuming axial periodicity. The computations provide values of the Reynolds numbers, wavenumbers, and wave speeds at the primary transition from Couette flow for radius ratios from 0.40–0.98. Particular attention has been focused on the bicritical curves that separate (as the magnitude of counter-rotation is increased) the transitions from Couette flow to flows with different azimuthal wavenumbers m and $m + 1$. This lays the foundation for further analysis of nonlinear mode interactions and pattern formation occurring along the bicritical curves and serves as a benchmark for experimental studies. Preliminary experimental measurements of transition Reynolds numbers and wave speeds presented here agree well with the computations from the mathematical model.

I. INTRODUCTION

Instabilities in flow between concentric rotating cylinders have been studied extensively since Taylor's classic theoretical and experimental work on the problem.[1] Although several investigators, including Taylor, have dealt with the general problem of independently rotating cylinders, much of the recent interest has focused on the succession of instabilities that occur as the inner cylinder speed is increased while the outer cylinder is held at rest.[2] Progress is made difficult by the fact that no analytic expressions exist for the flows that follow the basic laminar Couette flow. Davey et al.[3] succeeded in explaining the instability of Taylor vortices to nonaxisymmetic perturbations, but the analysis was performed in the small gap limit (i.e., the ratio of the radii of the cylinders was nearly equal to 1) and was strictly valid only in the neighborhood of the transition from Couette flow to Taylor vortices. More recently, numerical simulations have determined the structure of fully developed Taylor vortex flow and of wavy vortex flow, providing insight into mechanisms for instability and producing numerical results for such measurable properties as wave speeds (see, e.g., Refs. 4 and 5). The numerical approaches produce very detailed information about particular flows and promise to extend to higher instabilities. However, they are costly and exploration of a wide range of parameters is slow.

Thus it is worth reconsidering the possibilities for interesting dynamics in the neighborhood of the primary transition. Provided end effects are ignored, a simple expression can be written for the basic "Couette" flow and both analytic and numerical treatments of the flows following transition are much more tractable. The additional parameter obtained by rotating the outer cylinder makes possible a much greater variety of dynamics, as has been demonstrated by the extensive survey by Andereck et al.[6] Indeed, counter-rotation of the cylinders is known to produce a different primary instability: Instead of time-independent Taylor vortex flow, Couette flow gives way to spiral vortices, which are traveling waves in both the axial and azimuthal directions; see Fig. 1. The spiral vortex flow thus breaks both the continuous azimuthal and axial symmetries and is time periodic. Krueger et al.[7] showed with a linear stability analysis that for sufficiently rapid counter-rotation of the outer cylinder, laminar Couette flow becomes unstable first to a nonaxisymmetric mode. The computations of Krueger et al.[7] were performed in the small gap limit and for a limited set of parameters at finite gap; their narrow gap results were confirmed by the experiments of Snyder,[8] who also determined for four widely separated radius ratios (i.e., finite gap) the location of the bicritical points where Taylor vortices are replaced by spirals as the primary instability. A curve of these bicritical points was also produced in the numerical simulations of Jones.[4] DiPrima and Grannick[9] later considered the nonlinear problem of the growth of the nonaxisymmetric perturbations to finite amplitude.

This earlier work on flow between counter-rotating cylinders indicates that (i) for a given radius ratio there is a unique value of the outer cylinder speed beyond which the primary bifurcation is to nonaxisymmetric flows, (ii) the azimuthal wavenumber of the new flow increases as the outer cylinder speed becomes more negative, (iii) a nonlinear analysis is necessary to determine the exact symmetry of the resulting waveform (which may not be spiral) and distinguish between supercritical transitions (thus identifying possible hysteresis), and (iv) the regions of crossover from Taylor vortices to spirals or between spirals of different azimuthal wavenumbers may exhibit more complex dynamics as a result of interaction of several modes of flow. Most of the past work has either been restricted to the small gap limit or to a few parameter values for finite gaps; a comprehensive

---

[a] Permanent address: Department of Mathematics, University of Guelph, Guelph, Ontario N1G 2W1, Canada.
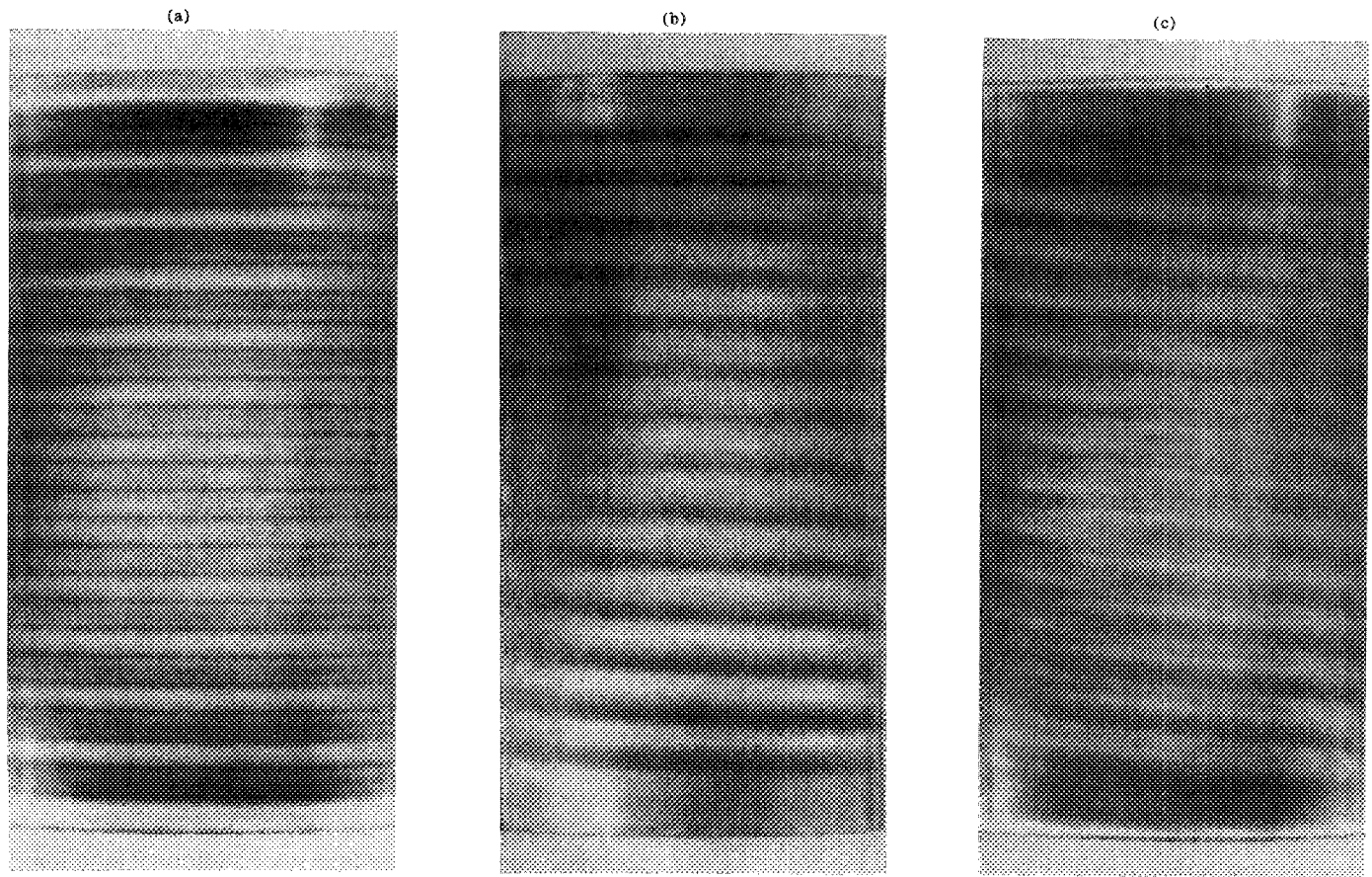[b] Permanent address: Department of Mathematics, University of Houston, Houston, Texas 77004.

FIG. 1. Flows branching from Couette flow for counter-rotating cylinders with radius ratio $\eta = 0.800$. (a) Taylor vortex flow ($R_2 = 0, R_1 = 97$). (b) Spiral vortex flow, $m = 1$ ($R_2 = -130, R_1 = 146$). (c) Spiral vortex flow, $m = 2$ ($R_2 = -150, R_1 = 156$).

quantitative view of the possibilities for a wide range of cylinder radius ratios and for several azimuthal wavenumbers remained lacking.

A fundamental problem in the Taylor–Couette experiment has been the explanation of the mechanism for the formation of the intriguing variety of patterns observed in the experiments. The recent bifurcation theory analysis of Chossat et al.[10] and Golubitsky and Stewart[11] suggest that the patterns can be explained in terms of mode interactions and the symmetry of the apparatus. For example, in Ref. 11, the flow patterns in the neighborhood of the bicritical primary transitions separating Taylor vortices and spirals were classified using group theoretic techniques. Patterns with symmetries corresponding to Taylor vortices, spirals, ribbons, wavy vortices, twisted vortices, and modulated periodic flows were found, most of which have been observed in experiments,[6] but not always at parameter values close to bicritical points. The question was left open as to which of these flow patterns are stable and can be expected to be observed under given experimental conditions. In this paper we present the necessary linear calculations, both analytical and numerical, required for specific predictions to be made. The nonlinear calculations, which determine the direction of branching and the stabilities of the solutions corresponding to the different flow patterns near this bicritical point, will be reported in a later paper.

A basic assumption in the theoretical model is that the flow is axially periodic, which implies that end effects can be neglected. In this paper we present detailed numerical work and preliminary experimental work that indicate that this assumption is a reasonable one, particularly in the neighborhood of the bicritical primary transition between Taylor vortices and spirals for sufficiently long cylinders.

The linear stability problem is formulated and the parameters and choice of scaling are given in Sec. II; the numerical approach used in the present work, including estimates of the accuracy of the computed results, are discussed in Sec. III; the results are described in Sec. IV; and the connection of the results to further work is discussed in Sec. V.

II. HYPOTHESES AND NOTATION

In 1923 Taylor[1] calculated the curve of neutral stability with respect to time-independent axisymmetric disturbances (that is, the $m = 0$ curve in our notation). Chandrasekhar[12] carried out an extensive analysis of the eigenvalue problem with $m = 0$. Later, neutral stability with respect to time-dependent nonaxisymmetric disturbances ($m > 0$) was computed by Krueger et al.[7] The case of $m > 0$ was also treated by Roberts,[13] but only for a fixed outer cylinder. Thus the linear stability analysis has long been well understood and needs

only be summarized here for the purpose of making clear the choices of the notation, scalings, and methods used in the present work.

With the mathematical idealization of infinitely long cylinders, there exists an exact solution of the Navier–Stokes equations, known as Couette flow, which satisfies the boundary conditions on the cylinder walls and is independent of the axial coordinate z. However, in real experiments in finite cylinders, the Ekman pumping at the ends produces a large cellular circulation for arbitrarily small cylinder rotation rates; hence the bifurcation to Taylor vortex flow is imperfect. On the other hand, the transition to spiral flow is a Hopf bifurcation, which is necessarily a perfect bifurcation.[14] The present work focuses on primary transitions occurring in the central region of a sufficiently long cylinder, where end effects appear to be of minor significance and the observed flow below criticality agrees closely with the ideal Couette flow.

In the mathematical model the physical boundary conditions are replaced by the assumption that the flow is periodic in the z direction, with period $2\pi/k$ (where k is the wavenumber). This introduces an additional variable k into the problem. The method of determining k from Taylor,[1] is to treat it as a continuous variable and to minimize the critical Reynolds number corresponding to inner cylinder rotation as a function of k, choosing the value that achieves this minimization, k_c. The numerical procedure for determining k_c is described in Sec. III.

An important consequence of the axial periodicity assumption is to introduce an additional symmetry into the problem. Axial periodicity means that axial translations are identified modulo $2\pi/k$. The Navier–Stokes equations, boundary conditions, and Couette flow solution are all invariant under these translations, as well as is the reflection $z \to -z$. Together these symmetries generate the group $O(2)$. These facts lead one to expect to find double eigenvalues of the linearized system, as can be seen from the following simple argument. Let $F(u) = 0$ represent the full Navier–Stokes boundary value problem. Then the symmetry properties described above can be expressed by

$$F(\gamma u) = \gamma F(u), \quad \forall \gamma \in O(2) . \tag{1}$$

Now linearize F by differentiation with respect to u and, since γ commutes with the differentiation operator, (1) becomes

$$D_u F(0)\cdot\gamma u = \gamma D_u F(0)\cdot u, \quad \forall \gamma \in O(2) , \tag{2}$$

that is, the derivative of F also commutes with elements of the group. Now suppose that λ is an eigenvalue of $D_u F(0)$, i.e.,

$$D_u F(0)v = \lambda v . \tag{3}$$

Then (2) implies

$$D_u F(0)(\gamma v) = \lambda(\gamma v), \quad \forall \gamma \in O(2) , \tag{4}$$

so that γv is also an eigenfunction corresponding to the same eigenvalue and the eigenspace is invariant under $O(2)$. Ge-

nerically then, it is either one- or two-dimensional. Experiments show that the bifurcation flows break the $O(2)$ symmetry, so the expected dimension is 2. The linear stability analysis confirms that all the critical eigenvalues are double. In the subsequent nonlinear analysis, the presence of this symmetry group has even more significant consequences. See Golubitsky and Stewart[11] for a more complete discussion of the effects of symmetry in Taylor–Couette flow.

The analysis begins with the Navier–Stokes equations for incompressible fluid flow:

$$\frac{\partial u}{\partial t} = \nu \nabla^2 u - (u\cdot\nabla)u - \frac{1}{\rho}\nabla p , \quad \nabla\cdot u = 0 , \tag{5}$$

where

$$\begin{aligned}
&u(r,t) = \text{the velocity vector at } r\in R^3 , \\
&p = \text{pressure} , \\
&\rho = \text{mass density} , \\
&\nu = \text{kinematic viscosity} .
\end{aligned} \tag{6}$$

The boundary conditions on the cylinder walls are the no-slip conditions, $u = $ cylinder velocity. The idealization that the flow is periodic in the axial coordinate z is equivalent to posing the problem in a finite cylinder of length $(2\pi/k)$, with periodic boundary conditions at the ends.

It is necessary to introduce some additional notation:

$$\begin{aligned}
&a = \text{inner cylinder radius}, \\
&b = \text{outer cylinder radius}, \\
&d = \text{gap width} = b - a, \\
&\eta = \text{radius ratio} = a/b, \\
&\Omega_1 = \text{inner cylinder angular velocity}, \\
&\Omega_2 = \text{outer cylinder angular velocity}, \\
&\mu = \Omega_2/\Omega_1 .
\end{aligned} \tag{7}$$

In the present work, $\Omega_1 > 0$ and $\Omega_2 < 0$. The Navier–Stokes equation (5) is brought into nondimensional form by rescaling the lengths by the gap width d, the velocity u by the inner cylinder velocity $a\Omega_1$, and time t by the quantity (d^2/ν). The separate time scale, although redundant, simplifies the analysis; physically, it is the time scale appropriate to the growth rate of the destabilizing modes. Then, in rescaled variables, (5) can be written as

$$\frac{\partial u}{\partial t} = \nabla^2 u - R_1(u\cdot\nabla)u - \nabla p , \quad \nabla\cdot u = 0 . \tag{8}$$

Here we define inner and outer cylinder Reynolds numbers R_1 and R_2 by

$$R_1 = a\Omega_1 d/\nu, \quad R_2 = b\Omega_2 d/\nu . \tag{9}$$

For purposes of comparison with previous work, we also define the angular speed ratio and Taylor number, respectively, by

$$\mu = \Omega_2/\Omega_1 = \eta R_2/R_1 ,$$
$$T = 4R_1(\eta R_1 - R_2)(1 - \eta)/[\eta(1 + \eta)] . \qquad (10)$$

In order to exploit the cylindrical geometry of the experiment, we introduce the cylindrical coordinates (r,θ,z) and the corresponding velocity components $\mathbf{u} = (u,v,w)$, where it is understood that r, z, u, v, and w are scaled to nondimensional variables, as above. The boundary conditions now take the form

inner cylinder: $r = \eta/(1 - \eta)$,

$u = 0, \quad v = 1, \quad w = 0 ,$

outer cylinder: $r = 1/(1 - \eta), \quad u = 0, \qquad (11)$

$v = \mu/\eta, \quad w = 0 ,$

axial periodicity: $\mathbf{u}(r,\theta,z) = \mathbf{u}(r,\theta,z + 2\pi/k) .$

We remark that the gap width is now equal to one and the axial wavenumber k is now in units of $1/d$.

The exact Couette flow solution of (8)–(11) is given by $\mathbf{u}_c = [0,v_c(r),0], p = p_c(r)$, where

$$p_c(r) = R_1 \int \frac{v_c^2}{r} dr , \quad v_c(r) = Ar + \frac{B}{r} , \qquad (12)$$

and

$$A = \frac{-(\eta^2 - \mu)}{\eta(1 + \eta)} , \quad B = \frac{\eta(1 - \mu)}{(1 - \eta)(1 - \eta^2)} . \qquad (13)$$

Quantities A and B correspond to the choice of nondimensional variables defined above; the classic quantities corresponding to the original physical variables in (6) are

$$\widetilde{A} = -\Omega_1\left(\frac{\eta^2 - \mu}{1 - \eta^2}\right) , \quad \widetilde{B} = a^2\Omega_1\left(\frac{1 - \mu}{1 - \eta^2}\right) . \qquad (14)$$

Next we transform the problem (8)–(11) to one for the deviation from Couette flow by substituting

$$\mathbf{u} = \mathbf{u}_c + \hat{\mathbf{u}} , \quad p = p_c + \hat{p} \qquad (15)$$

and then dropping the carets. The resulting equations, written out explicitly in cylindrical coordinates, are

$$u_t = \nabla^2 u - \frac{u}{r^2} - \frac{2}{r^2} v_\theta - p_r - C(r)(u_\theta - 2v)$$
$$- R_1\left(uu_r + \frac{v}{r} u_\theta + wu_z - \frac{v^2}{r}\right) ,$$

$$v_t = \nabla^2 v - \frac{v}{r^2} + \frac{2}{r^2} u_\theta - \frac{1}{r} p_\theta + 2Du - C(r)v_\theta \qquad (16)$$
$$- R_1\left(uv_r + \frac{v}{r} v_\theta + wv_z + \frac{uv}{r}\right) ,$$

$$w_t = \nabla^2 w - p_z - C(r)w_\theta - R_1[uw_r + (v/r)w_\theta + ww_z] ,$$

$$u_r + (1/r)u + (1/r)v_\theta + w_z = 0 ,$$

where the t, r, θ, and z subscripts indicate partial derivatives. Here we have introduced the constant D and the nonconstant coefficient $C(r)$ defined by

$$D = -R_1A = (\eta R_1 - R_2)/(1 + \eta) > 0 ,$$

$$C(r) = R_1\left(A + \frac{B}{r^2}\right) \qquad (17)$$
$$= -D + \left(\frac{\eta}{1 - \eta}\right)\left(\frac{R_1 - \eta R_2}{1 - \eta^2}\right)\left(\frac{1}{r^2}\right) .$$

The boundary conditions for (16) are

$u = v = w = 0,$

at $r = \eta/(1 - \eta)$ and $r = 1/(1 - \eta) ,$
$$(18)$$

as well as being $2\pi/k$ periodic in z and 2π periodic in θ.

The stability of the Couette solution $\mathbf{u}$ is calculated from the linearization about $\mathbf{u}_c$ in (8) or the linearization about $\mathbf{u} = 0$ in (16):

$$u_t = \nabla^2 u - u/r^2 - (2/r^2)v_\theta - p_r + 2C(r)v - C(r)u_\theta ,$$
$$v_t = \nabla^2 v - v/r^2 + (2/r^2)u_\theta - (1/r)p_\theta + 2Du - C(r)v_\theta ,$$
$$w_t = \nabla^2 w - p_z - C(r)w_\theta , \qquad (19)$$
$$u_r + (1/r)u + (1/r)v_\theta + w_z = 0 .$$

Asymptotic stability of (19) is determined by the eigenvalues of the operator defined by the right-hand side of (19). These eigenvalues and the corresponding eigenfunctions have been calculated by substituting into (19) the ansatz

$$u = U(r)\exp[i(kz + m\theta) + \sigma t] ,$$
$$v = V(r)\exp[i(kz + m\theta) + \sigma t] ,$$
$$w = W(r)\exp\{i[kz + (\pi/2) + m\theta] + \sigma t\} , \qquad (20)$$
$$p = P(r)\exp[i(kz + m\theta) + \sigma t] .$$

Here σ is the eigenvalue, possibly complex, and m is the azimuthal wavenumber, either 0 (axisymmetric case) or a positive integer (nonaxisymmetric). The phase shift of $i\pi/2$ in the w component has the mathematical consequence that Eq. (21) is purely real in the case $m = 0$. The result after substitution is

$$\sigma U = U'' + \frac{1}{r} U' - [(1 + m^2)/r^2 + k^2]U + 2C(r)V$$
$$- P' - im[(2/r^2)V + C(r)U] ,$$
$$\sigma V = V'' + (1/r) V' - [(1 + m^2)/r^2 + k^2]V + 2DU$$
$$- (im/r)P + im[(2/r^2)U - C(r)V] , \qquad (21)$$
$$\sigma W = W'' + (1/r)W' - (m^2/r^2 + k^2)W - kP$$
$$- imC(r)W ,$$
$$U' + (1/r)U + (im/r)V - kW = 0 ,$$

where the primes denote derivatives with respect to r.

The final step of the simplification is to eliminate the pressure P from (21) by means of a classical trick involving the continuity equation; see Roberts.[14] Define a new dependent variable $X(r)$ by

$$X = U' + (1/r)U - P . \qquad (22)$$

From the continuity equation one obtains

$$P = -X + kW - (im/r)V, \qquad (23)$$

which is used to eliminate P from the second and third equations of (21), while the derivative of (22) is used to eliminate P' from the first equation.

For the numerical analysis, it is preferable to work with a system of first-order equations, rather than second-order equations. Therefore, we introduce two more new variables

$$Y = V' + (1/r)V, \quad Z = W', \qquad (24)$$

so that (21) can be written as the eigenvalue problem

$$U' = -(1/r)U + kW - (im/r)V,$$

$$V' = -(1/r)V + Y,$$

$$W' = Z,$$

$$X' = \sigma U + (m^2/r^2 + k^2)U - 2C(r)V$$
$$+ im[(2/r^2)V + C(r)U],$$

$$Y' = \sigma V + \left(\frac{2m^2}{r^2} + k^2\right)V - 2DU \qquad (25)$$
$$+ im\left(\frac{-2}{r^2}U + C(r)V + \frac{k}{r}W - \frac{1}{r}X\right),$$

$$Z' = \sigma W + (m^2/r^2 + 2k^2)W - (1/r)Z - kX$$
$$+ im[-(k/r)V + C(r)W],$$

with the boundary conditions

$$U = V = W = 0, \quad \text{at } r = \eta/(1-\eta), 1/(1-\eta). \qquad (26)$$

For neutral stability we are interested only in the cases with eigenvalue $\sigma = 0$ or $\sigma = i\omega$ (pure imaginary). The eigenvalue problem (25) and (26) has been solved numerically, as described in Sec. III.

Equations (25) and (26) possess a symmetry in that they are unchanged by the substitution $(k,W,Z) \to (-k, -W, -Z)$. This corresponds physically to a reflection of the apparatus in the axial direction; $z \to -z$. Mathematically, this symmetry implies that for any given solution of (25) and (26) for k, there corresponds another solution for $-k$. In the real case this means that solutions occur in pairs. In the complex case, solutions of (25) and (26) occur in quadruples corresponding to $\pm k$ and the two complex conjugates. This is in accord with the earlier remarks concerning symmetry.

III. NUMERICAL PROCEDURES

In Sec. II the study of the Navier–Stokes partial differential equation was reduced to that of an ordinary differential equation eigenvalue problem (25) and (26). Standard techniques are available for the numerical solution of such two-point boundary value problems,[15] so the procedure need only be sketched here. The main difference between these calculations and those performed in the 1960's and 1970's is the advancement in computer technology, which makes it possible to perform more extensive calculations on personal computers than could have been done on mainframe computers of that era.

The numerical investigation of the eigenvalue problem (25) and (26) separates naturally into two distinct cases; the real case with $m = 0$ (axisymmetric) and the complex case with $m > 0$ (nonaxisymmetric). In both cases, the eigenvalue problem was solved by a shooting method using a standard fourth-order Runge–Kutta integrator for the differential equations and quasi-Newton iteration for the eigenvalue condition. All computations were done in double precision (64 bits) and selected calculations were repeated with smaller step sizes as a check on accuracy. Normally, the eigenfunctions were computed with 100 equally spaced steps in the interval. This approach was chosen over finite difference or collocation approaches because of the ease with which it gives high-order accurate results on small computers. In all cases, tests with smaller step sizes showed the numerical accuracy to be at least four digits, which was deemed adequate for comparison with experimental data.

In the axisymmetric ($m = 0$) case, as noted previously, the eigenvalue problem becomes real. The procedure was to input values of k, η, and R_2; fix $\sigma = 0$ (for neutral stability); and then solve the resulting eigenvalue problem for R_1 by quasi-Newton iteration. [Note that k, R_1, and R_2 enter (25) only through the coefficients C and D defined in (17).] This calculation was repeated using a mesh of values of k until a minimum of R_1 vs k was detected. The actual minimizing value of k, k_c, and the corresponding R_1 were then determined by quadratic interpolation.

In the nonaxisymmetric ($m > 0$) case, the complex six-dimensional system (25) and (26) was rewritten as a 12-dimensional real system and the solution computed as before, except that we set $\sigma = i\omega$ (for neutral stability) and performed quasi-Newton iteration to find R_1 and ω simultaneously from the complex eigenvalue condition. Note that ω has a useful physical interpretation as the azimuthal wave speed. The minimization algorithm to find the critical axial wavenumber k_c was the same as in the $m = 0$ case.

The derivative with respect to R_1 (and with respect to ω in the $m > 0$ case), required for Newton iteration, was computed in the two different ways. The first was simply divided differences recomputed every third iteration. This method was found to be numerically unstable at smaller values of the radius ratio η. The second method, which was found to be more stable, was numerical integration (again by shooting) of the linear variational equations satisfied by the R_1 and ω derivatives of the solution.

Initially, these calculations were performed on IBM-PC class microcomputers with 8087 numeric coprocessors (on which each curve in Fig. 4 took up to 8 h). Later calculations were performed on a Ridge 32 minicomputer, which completed the same calculations in minutes.

IV. RESULTS

The principal results are graphed in Figs. 2 and 3, which show the regions in the (R_2,η) and (μ,η) planes, respectively, in which secondary flows of different azimuthal wavenumbers are predicted to appear. The boundaries of the regions are of special interest since it is in their vicinity that mode interaction might be expected. At these boundaries, modes of two different wavenumbers are unstable simultaneously; consequently, we refer to points on the boundaries as bicritical points. Since they are in general obtainable only by variation of two parameters, they are also referred to in
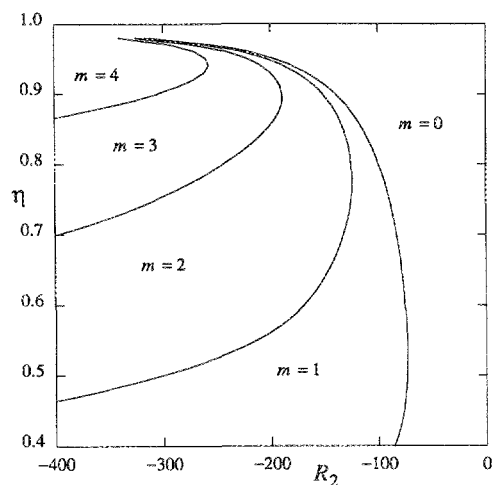
FIG. 2. Regions in the (R_2, η) plane in which different azimuthal wavenumbers m are selected when Couette flow becomes unstable as R_1 is increased. Bicriticality occurs at the curves separating the regions.

the language of bifurcation theory as codimension-2 points.

It should be emphasized that Figs. 2 and 3 represent the results of linear theory only. As was pointed out by Krueger et al.[7] and investigated for a limited selection of parameters by Di Prima and Grannick,[9] the exact spatial symmetry of the nonaxisymmetric flows ($m \neq 0$) remains undetermined by the linear theory. Also undetermined is the effect of subcritical bifurcations, which might have the result that a subcritically unstable mode is seen experimentally instead of the mode expected from linear theory. The subcritical behavior of the axisymmetric flows has been examined numerically by Jones.[4] The results from the nonlinear theory and from numerical simulations over the wide parameter range considered here will follow in later papers, in which modifications of Figs. 2 and 3 will be presented.

In the linear stability computations, R_2 was restricted to be greater than -400 for two reasons: (i) several changes in azimuthal wavenumber have already occurred by this point, thus producing many possibilities for mode interaction; and (ii) experiments[8] show that end effects become significant
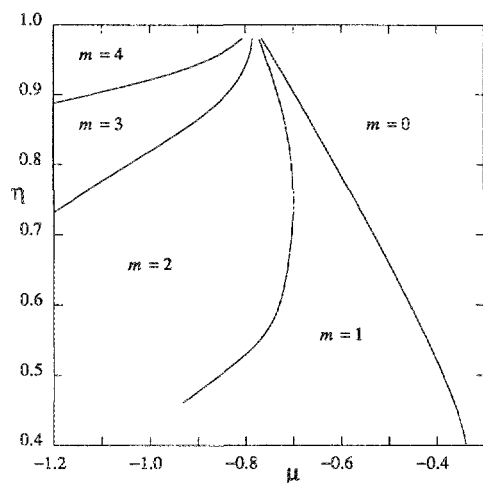

FIG. 3. Regions in the (μ, η) plane in which different azimuthal wavenumbers m are selected when Couette flow becomes unstable as T is increased. As in Fig. 2, bicriticality occurs in the curves separating the regions. Note the convergence of the curves as $\eta \to 1$.

for $R_2 < -400$. The radius ratio was restricted to be greater than 0.4 because precise experimental systems have been constructed more often for larger radius ratios (smaller gaps). Moreover, for counter-rotating flows with wide gaps, the interesting dynamics occurs near the inner cylinder and is difficult to observe. Finally, the azimuthal wavenumber was restricted to values of less than 5; higher values of the azimuthal wavenumber might appear as regions in the upper left-hand corners of Figs. 2 and 3, i.e., for radius ratio close to 1 and R_2 near -400.

Within these limits there are many regularities to be observed. At constant radius ratio (i.e., for a given experimental apparatus), regions occupied by successive nonzero values of m span wider ranges of R_2 or μ. It appears that the variation of m with R_2 is monotonic, i.e., there do not appear to be any cases where a lower value of m reappears as R_2 is made more negative. The boundary curves in the (R_2, η) plane are bowed, so for any given jump in wavenumbers there is a value of the radius ratio such that the jump occurs at a minimum value of R_2. Also note the confluence of the multicritical curves as the radius ratio approaches unity (small gap limit). The asymptotic behavior in Fig. 3 is consistent with the small gap calculations of Krueger et al.[7]

Finally, one way to view Fig. 2 is as the projection onto the (R_2, η) plane of the intersection of surfaces in the three-dimensional (R_1, R_2, η) parameter space, across which a mode of azimuthal wavenumber m first becomes unstable for some axial wavenumber k. Similarly, Fig. 3 is the projection onto the (μ, η) plane of instability surfaces in the (T, μ, η) parameter space.

Experiments are performed at fixed radius ratio. Transition is typically found in one of two ways: (i) one cylinder
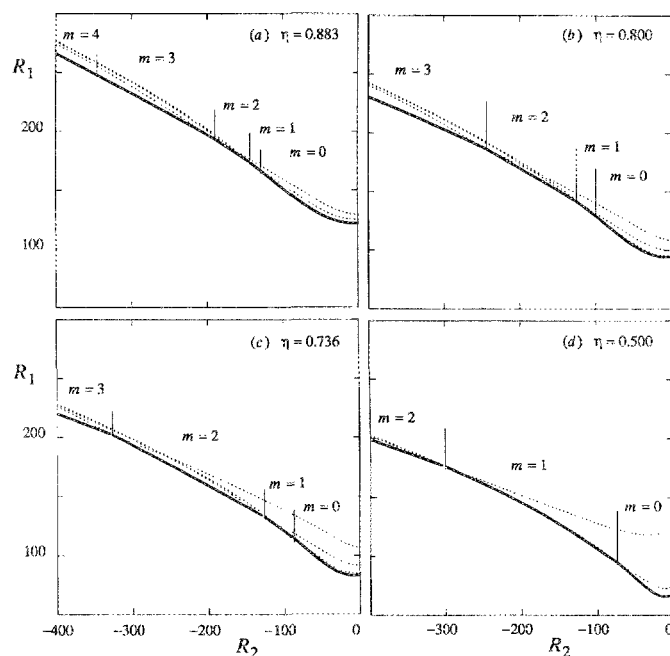

FIG. 4. Critical values of R_1 as a function of R_2. (a) $\eta = 0.883$, (b) $\eta = 0.800$, (c) $\eta = 0.736$, and (d) $\eta = 0.500$. Separate curves are for different values of the azimuthal wavenumbers m. The solid curve is the envelope defined by the smallest critical value of R_1 for all possible values of m.
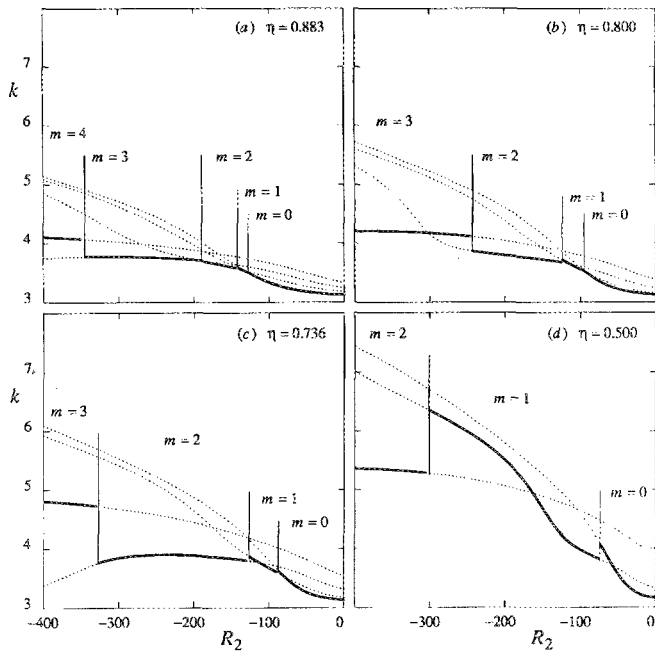
FIG. 5. Axial wavenumber as a function of R_2 when R_1 is at its critical value for (a) $\eta = 0.883$, (b) $\eta = 0.800$, (c) $\eta = 0.736$, and (d) $\eta = 0.500$. Each curve represents a different value of m. The solid portions identify the values corresponding to the smallest critical R_1.

FIG. 6. Wave speed as a function of R_2 when R_1 is at its critical value for (a) $\eta = 0.883$, (b) $\eta = 0.800$, (c) $\eta = 0.736$, and (d) $\eta = 0.500$. Each curve represents a different value of m. The solid portions identify the value corresponding to the smallest critical R_1.

speed is held constant (usually the outer) and the other cylinder speed is adjusted until transition is observed, (ii) the speed ratio μ is held fixed and T is varied. After transition occurs, experiments can measure m, k, and (if the flow is time periodic) ω. Following the first approach, for radius ratios stepped in increments of 0.05, we have tabulated the following for each value of m and for R_2 varying from 0 to -400: R_1, μ, T, k, and ω/Ω_1. These tables have been deposited with the publisher[16] and are also available from the authors. The scaling of the data is as explained in Sec. II. Similar data for two radius ratios ($\eta = 0.95$ and 0.752) were computed by Demay and Iooss[10]; the results agree to within 0.1%.

The tabulated results have been used to generate the plots of Figs. 4–6. Here for the radius ratios 0.883, 0.800, 0.736, and 0.500 are plotted curves of the transition inner Reynolds number versus outer Reynolds number (Fig. 4); axial wavenumber versus outer Reynolds number (Fig. 5); and azimuthal wave speed versus outer Reynolds number (Fig. 6). A different curve is drawn for each value of the azimuthal wavenumber m. The solid portions of the curves identify the values corresponding to the lowest critical R_1; these are the values that linear stability theory predicts should be seen in experiment.

Consider first Figs. 4(a)–4(d). Following the solid portion of the curves, the predicted transition Reynolds numbers form by definition a continuous curve; the azimuthal wavenumbers change where the curves for individual values of m cross. There are, however, discontinuities in the slope of this transition curve at the crossing point. The curves for each value of m remain close to one another, so that the crossings are nearly tangent. The numerical values
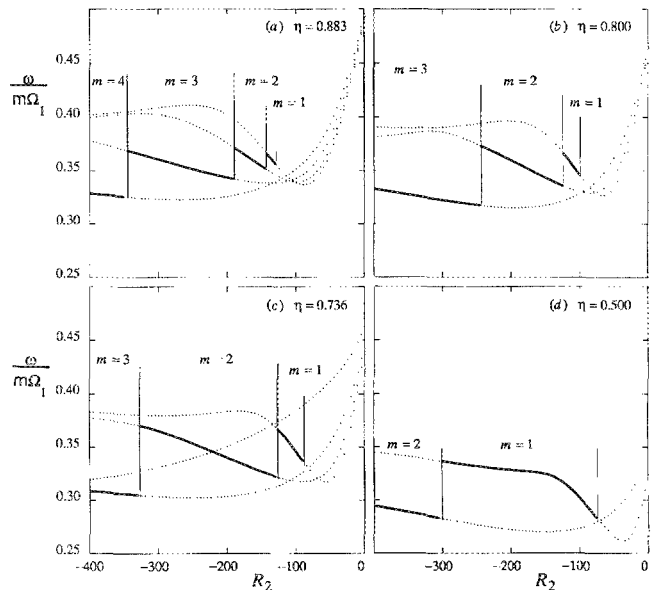
of the crossings, i.e., the bicritical points, are in Table I. A more complete table for many other radius ratios has been deposited with the American Institute of Physics Auxiliary Publication Service (PAPS).[16]

There is a weak minimum in the predicted transition curve that always occurs for the Taylor vortex flow state. Beyond this minimum, the curves climb upward so that by $R_2 = -400$, the critical value for R_1 is more than twice that at $R_2 = 0$. This appears to be the case for all of the radius ratios studied, although there is a downward shift of the curves as η is decreased. Rotation of the outer cylinder is seen to be at first weakly destabilizing, but soon becomes stabilizing. Experimental data are compared to the computed transition Reynolds numbers in Fig. 7.

Next consider Figs. 5(a)–5(d), which show the axial wavenumber k (normalized by the full gap width d) versus R_2. Here is it seen that there are discontinuities in k at the points where the azimuthal wavenumber changes. The size of the discontinuities increases as m becomes larger. It also increases for a given multicritical point as the radius ratio decreases. Note that the jumps are toward decreasing wavenumber for the transitions $0 \rightarrow 1$ and $1 \rightarrow 2$, but then toward increasing wavenumber for $2 \rightarrow 3$ and $3 \rightarrow 4$. The wavenumber increases as R_2 becomes more negative. This is to be expected since the gap over which the basic flow is centrifugally unstable (in the inviscid limit) becomes narrower as R_2 becomes more negative.

Finally, Figs. 6(a)–6(d) present wave speed versus R_2, where the wave speed is normalized by the inner cylinder speed Ω_1. The wave speed ($\omega/m\Omega_1$) is plotted rather than frequency (ω/Ω_1) in order to examine the extent to which the waves are dispersionless with respect to azimuthal wavenumber. The wave speeds stay within a confined range (between 0.3 and 0.4), but there are discontinuities when m

TABLE I. Bicritical points computed for the radius ratios used in Figs. 4–6; also included are the wavenumbers and wave speeds at the bicritical points.

$m \to m+1$	R_2	R_1	μ	T	k_m	k_{m+1}	$\omega_m/m\Omega_1$	$\omega_{m+1}/(m+1)\Omega_1$
$\eta = 0.500$								
$0 \to 1$	-73.79	95.25	-0.3874	30 842	4.079	3.813	0	0.2813
$1 \to 2$	-300.85	175.94	-0.8550	182 420	6.354	5.280	0.3365	0.2825
$\eta = 0.736$								
$0 \to 1$	-87.71	114.82	-0.5622	16 344	3.631	3.590	0	0.3345
$1 \to 2$	-126.45	132.91	-0.7004	24 611	3.872	3.796	0.3670	0.3216
$2 \to 3$	-326.98	202.37	-1.1890	79 518	3.765	4.722	0.3702	0.3047
$\eta = 0.800$								
$0 \to 1$	-99.25	129.55	-0.6129	14 603	3.571	3.551	0	0.3445
$1 \to 2$	-124.60	141.80	-0.7030	18 751	3.726	3.678	0.3663	0.3355
$2 \to 3$	-243.40	186.67	-1.0430	40 729	3.871	4.114	0.3731	0.3174
$\eta = 0.883$								
$0 \to 1$	-128.93	166.88	-0.6822	12 978	3.516	3.511	0	0.3546
$1 \to 2$	-142.81	173.83	-0.7254	14 498	3.592	3.574	0.3654	0.3505
$2 \to 3$	-189.68	193.78	-0.8643	19 679	3.704	3.708	0.3711	0.3418
$3 \to 4$	-345.74	248.16	-1.2300	39 456	3.779	4.070	0.3688	0.3253

changes. (If the wave speed were dispersionless, not only would there be no jumps, but also all of the curves for different values of m would collapse onto one another.) The jumps increase with increasing m for fixed radius ratio and also increase with decreasing radius ratio for fixed $m_1 \to m_2$.

Since this work has been motivated by the desire to identify multicritical points, it is important to check how well experiments agree with the predictions for the location of the multicritical points, wave speeds, and wavenumbers. Table II contains the results of experimental observations for radius ratio 0.8. The differences between theory and experiment are within the experimental uncertainties. Observations at other radius ratios are in progress. The relatively large uncertainties associated with wave speed and wavenumber has prompted further study, some early results of which are given in Table III. As shown in Fig. 8, the wave speeds fall off rapidly as the Reynolds number R_1 is increased above critical. When care is taken to select the wave speed measured closest to transition, agreement with linear theory is excellent. A systematic nonlinear analysis of wave speeds and wavenumbers at and above transition is now under way.
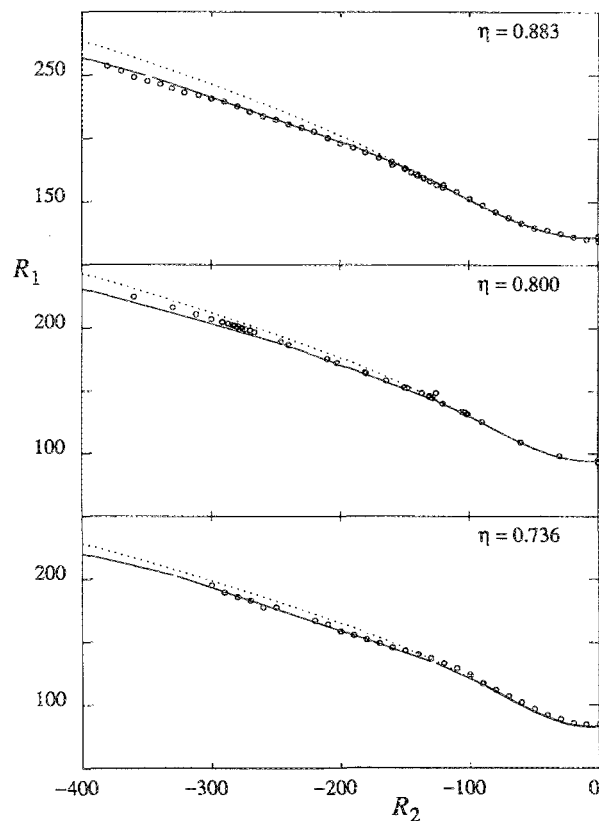

FIG. 7. Experimentally determined critical values of R_1 for radius ratios $\eta = 0.883$, $\eta = 0.800$, and $\eta = 0.736$. The solid curves are the theoretical envelopes of the lowest critical R_1 for all possible m. The dotted curves are the theoretical values of R_1 for $m = 0$.

TABLE II. Comparison of experimental and theoretical results at bicritical points for radius ratio $\eta = 0.80$. For the experimental data the aspect ratio was 30. The experimental uncertainties are about 1% in Reynolds number, 5% in wavenumber, and 2% in wave speed.

	Theoretical	Experimental	Difference
$m = 0$ to $m = 1$ bicritical point			
R_2	-99.2	-100.7	-1.5%
R_1	129.5	131.0	1.1%
μ	-0.613	-0.615	-0.3%
k_0	3.57	3.59	0.6%
k_1	3.55	3.49	-1.7%
ω_1/Ω_1	0.345	0.339	-1.8%
$m = 1$ to $m = 2$ bicritical point			
R_2	-124.6	-130.2	-4.3%
R_1	141.8	145.3	2.4%
μ	-0.703	-0.717	-2.0%
k_1	3.73	3.55	-5.1%
k_2	3.68	3.78	2.7%
ω_1/Ω_1	0.366	0.364	-0.5%
$\omega_2/2\Omega_1$	0.335	0.332	-0.9%

TABLE III. Comparison of theoretical and experimental critical wave speed values for radius ratio $\eta = 0.883$. Experimental uncertainties are about 1% in Reynolds number and wave speed.

R_2	m	Theoretical $\omega_m/m\Omega_1$	Experimental $\omega_m/m\Omega_1$	Difference
-155	2	0.3561	0.354	0.6%
-220	3	0.3462	0.346	0.0%
-225	3	0.3470	0.350	0.9%
-250	3	0.3512	0.349	0.6%
-255	3	0.3521	0.353	0.3%
-260	3	0.3530	0.354	0.3%
-300	3	0.3604	0.361	0.2%

FIG. 8. Wave speed of spirals for R_1 varying through its critical value (with $\eta = 0.800$ and $R_2 = -152.15$). Circles are data taken while increasing R_1 and crosses are data taken while decreasing R_1. The square is the result from the linear stability computations at onset. The wave speeds are derived from a time-varying signal produced by detection of laser light reflected from the flow visualization material. With the exception of the data points at $R_1 = 151.8$, where the signal is extremely weak, the wave speeds decrease monotonically with increasing R_1.

V. DISCUSSION

Figures 2–8 (and the corresponding tables on deposit with the publisher[16]) provide a comprehensive survey of the primary transitions from Couette flow over a wide range of the parameters R_1, R_2, and η for counter-rotating cylinders. Special attention was given to the multicritical curves, where two modes go unstable simultaneously in the three-dimensional parameter space. This body of data will provide the basis for further studies, both theoretical and experimental, of multicritical phenomena in the Taylor–Couette system.

Recent advances in the mathematical theory of multicritical phenomena and equivariant bifurcation theory have led to a new qualitative explanation of pattern formation and of transitions leading to complex dynamics in a wide variety of systems. The Taylor–Couette system is one of the few systems governed by partial differential equations for which it is possible to calculate explicitly the predictions of these theories for multicritical phenomena and to test them experimentally. The emphasis in our work is quantitative rather than qualitative in order to make rigorous tests of these new mathematical theories. The quantities that have been tabulated (Reynolds numbers, wavelengths, and wave speeds) are all readily measured experimentally. The results of this work will have relevance, not only for Taylor–Couette flow, but for any system exhibiting multicriticality and symmetry. The agreement found in preliminary experimental work on the location of the $m = 0$ to $m = 1$ transition and associated wavelength and wave speed values (Tables II and III) supports further theoretical investigations based on the assumption of axial periodicity.

These numerical results have already guided the experiments in new directions and have led to new insights. For example, Figs. 2 and 3 show that investigation of the $m = 0$ to $m = 1$ transition for narrow gaps is more likely to encounter interference with modes having higher m values than the same transition for wider gaps (smaller η). Therefore, the experimental work has moved away from an apparatus with $\eta = 0.883$ to others with $\eta = 0.800$, 0.736, and 0.500. Guided by the maps of multicritical curves presented here, experiments have already found effects unnoticed previously, such as the early onset of secondary bifurcations and hysteresis near the primary transition. These nonlinear phenomena will be reported in a later paper.
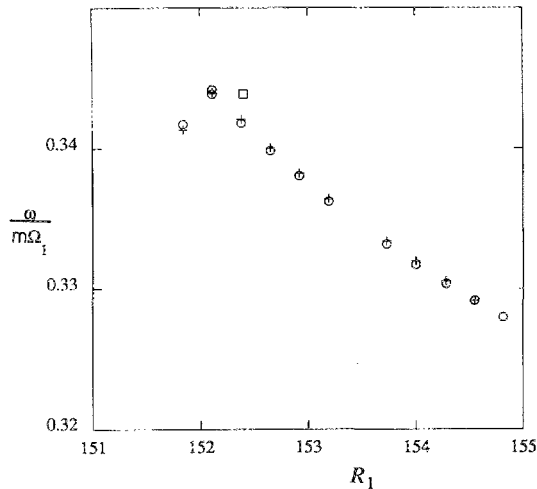
[1]G. I. Taylor, Philos. Trans. R. Soc. London Ser. A **223**, 289 (1923).

[2]R. C. Di Prima and H. L. Swinney, in *Hydrodynamic Instabilities and the Transition to Turbulence*, edited by H. L. Swinney and J. P. Gollub (Springer, Berlin, 1985), 2nd ed., p. 139.

[3]A. Davey, R. C. Di Prima, and J. T. Stuart, J. Fluid Mech. **31**, 17 (1968).

[4]C. A. Jones, J. Fluid Mech. **102**, 249 (1981); **120**, 433 (1982); **157**, 135 (1985).

[5]P. S. Marcus, J. Fluid Mech. **146**, 45, 65 (1984).

[6]C. D. Andereck, S. S. Liu, and H. L. Swinney, J. Fluid Mech. **164**, 155 (1986).

[7]E. R. Krueger, A. Gross, and R. C. Di Prima, J. Fluid Mech. **24**, 521 (1966).

[8]H. A. Snyder, Phys. Fluids **11**, 728, 1599 (1968); Int. J. Non-Linear Mech. **5**, 659 (1970).

[9]R. C. Di Prima and R. N. Grannick, in *Instability of Continuous Systems*, edited by H. Leipholz (Springer, Berlin, 1971), p. 55.

[10]Y. DeMay and G. Iooss, J. Méc. Theor. Appl. Numéro special 193, (1984); P. Chossat and G. Iooss, Jpn. J. Appl. Math. **2**, 37 (1985); P. Chossat, Y. DeMay, and G. Iooss, Arch. Rat. Mech. Anal. **99**, 213 (1987).

[11]M. Golubitsky and I. Stewart, SIAM J. Math. Anal. **17**, 249 (1986).

[12]S. Chandrasekhar, *Hydrodynamic and Hydromagnetic Stability* (Oxford U. P., London, 1961).

[13]P. H. Roberts, Proc. R. Soc. London Ser. A **283**, 531 (1965), Appendix.

[14]M. Golubitsky and D. G. Schaeffer, *Singularities and Groups in Bifurcation Theory: Vol. 1* (Springer, New York, 1985).

[15]H. B. Keller, *Numerical Methods for Two-Point Boundary Value Problems* (Blaisdell, Waltham, MA, 1968).

[16]See AIP document no. PAPS PFLDA-31-776-41 for five pages of bicritical point data and 39 pages of critical Reynolds numbers, wavenumbers, and wave speeds. Order by PAPS number and journal reference from American Institute of Physics, Physics Auxiliary Publication Service, 335 East 45th Street, New York, NY 10017. The price is $1.50 for each microfiche (98 pages) or $5.00 for photocopies of up to 30 pages and $0.15 for each additional page over 30 pages. Airmail additional. Make checks payable to the American Institute of Physics.